

Experimental Inquiry and Machine Learning for Predictive Analysis of Friction Stir Welded AA5052 and AZ31B Dissimilar Joints

Subi. B, Padmanaban Ramasamy*

* dr_padmanaban@cb.amrita.edu

¹ Department of Mechanical Engineering, Amrita School of Engineering, Coimbatore, Amrita Vishwa Vidyapeetham, India

Received: January 2024

Revised: April 2024

Accepted: May 2024

DOI: 10.22068/ijmse.3491

Abstract: The present investigation delves into the friction stir welding of AA5052 and AZ31B alloys, examining the effects of three distinct parameter configurations. A face-centered central composite design, structured to incorporate full replications for comprehensive and reliable analysis, was employed. A pivotal element of this study is implementing an advanced deep neural network (DNN) model. Characterized by its varied activation functions, structural parameters, and training algorithms, this DNN model was adeptly configured to precisely predict the tensile strength and microhardness of the welded joints. This comprehensive examination also included a quantitative assessment of the parameter effects on joint microstructure and mechanical properties. Flawless welds with exemplary surface characteristics were attained through a meticulously optimized set of parameters: a tool rotation speed set at 825 rpm, a tool traverse speed of 15 mm/min, and a shoulder diameter of 18 mm. During the welding process, the formation of intermetallic compounds, specifically $Al_{12}Mg_{17}$ and Al_3Mg_2 , was observed. An exceptionally refined grain size of $2.23 \mu m$ was observed in the stir zone, contributing to the joint's enhanced tensile strength, measured at 180 MPa. The hardness of the specimen fabricated at the high rotational speed is more elevated due to the brittle intermetallic compounds. The better mechanical properties are related to the reduction and distribution of intermetallic compounds formed in the interface zone.

Keywords: Friction stir welding, AA5052, AZ31B, Microstructure, Mechanical properties, Neural Network.

1. INTRODUCTION

Contemporary automobile, aerospace, and shipbuilding industries emphasize lightweighting, emissions reduction, and performance enhancement [1]. The European Union, for instance, aims to reduce greenhouse gas emissions by 40% by 2030, with a critical insight that a 10% decrease in vehicle mass can result in a 5-8% reduction in specific fuel consumption [2, 3]. Utilizing Al-Mg material combinations succors lightweighting, enhances fuel efficiency, and curtails environmental impact [4]. Al-Mg joint applications span diverse domains, including aerospace, automobile manufacturing, marine engineering, airship propulsion systems, atomic reactor materials, and X-ray gear components [5].

Conventional fusion welding methods are often futile when joining dissimilar materials due to excessive heat input, solidification defects, macro segregation, and the creation of fragile intermetallic compounds (IMC) [6]. For instance, the Al-Cu combination forms IMC phases and eutectics at temperatures exceeding $1200^{\circ}C$ [7]. The conventional welding of the Al-Mg

combination is plagued by issues like grain coarsening, cracking, void formation, and IMC formation at the interface [8].

Friction stir welding (FSW) is a highly effective approach to dissimilar materials without degrading properties [9]. In FSW, the plasticized material flow and mechanical interlocking enhance atomic diffusion and mitigate welding defects, facilitating the formation of metallurgical bonds between closely contacted metal surfaces under high loads and shear strains [4],[8],[10].

Heidarzadeh et al. [11] elucidated that the transfer of Fe and Cr from the tool and the creation of nano-sized compounds of intermetallic hindered the dislocation mobility during FSW of Cu-Zn alloy, resulting in the formation of finer grains and increased joint strength. Fazel et al. report that material flow increases with tool rotation speed in lap joints, albeit beyond a certain speed, which leads to weak joints due to incomplete material mixing [10]. Padmanaban et al. determined that FSW of aluminum alloys achieves sound joints with a high tensile strength at specific tool rotation and shoulder diameter combinations [12]. Other studies delve into factors affecting FSW outcomes. Firdouzdor et al. observed the

formation of interface intermetallic compounds due to increased heat input at high rotation speeds in Al-Mg friction stir-welded joints [13]. Malarvizhi et al. established that for dissimilar FSW, especially Al to Mg combinations, slightly higher heat input is necessary to facilitate proper material mixing, advocating for a specific shoulder diameter [14]. Fu et al. proposed a range of parameters for defect-free joints between Al-Mg [15].

Padmanaban et al. [22] also emphasized by using the numerical method that material flow and heat input increase with tool rotation speed and shoulder diameter. Ratna Kishore et al. also found that viscous dissipation generates maximum heat at the harder material side [17]. Baghdadi et al. obtained a defect-free weld between AZ31B & Al6061-T6 with good mechanical properties at TRS of 600 rpm and TTS of 20 mm/min by placing Al on the retreating side [4]. Zhao et al. explored the FSW of Al-Ti for various probe lengths and found that the formation of fragile IMCs is high when the probe length is above the optimum probe length (3.1 mm), resulting in the fracture at the interface [18].

Studies suggest that high tool rotation and too low transverse speed can result in IMC formation. In contrast, a medium range of parameters is preferred for sound welds [19]. Techniques such as Taguchi and response surface methodology have been extensively used for modelling the FSW process. However, artificial neural networks (ANNs) have demonstrated superiority in creating nonlinear mathematical models and establishing correlations between inputs and outputs [21, 22, 23]. Ai et al. [24] successfully established correlations between input process parameters and geometric characteristics of weld-seam in laser welding using RBFNN. Pal et al. extended this success by developing distinct RBFNN models to predict welded plate distortion, with the most effective model achieving a mere 5.56% prediction error [25]. Pramod et al. [26] developed an ANN model to forecast the wear properties of Al71075/Al₂O₃ composites, and the model demonstrated strong agreement with experimental findings. Tyagi et al. [27] evaluated the accuracy of ANN and Response Surface Methodology (RSM) prediction models for forecasting the wear properties of composites produced through FSP, noting that both models closely approximated

experimental data.

In this research, the potential of ANNs is used to simulate the effect of the FSW process parameters, namely tool rotation speed, tool traverse speed, and tool shoulder diameter on Microstructure, Microhardness, and tensile strength in Al-Mg alloy joints.

2. EXPERIMENTAL PROCEDURES

The study used commercially available AA5052 alloy and AZ31B alloy sheets (150 × 50 × 4 mm). The FSW process is carried out on a modified vertical milling machine. Three HCHCR tools with shoulder diameters of 15, 18, and 21 mm were used. The length of the pin was 3.6 mm, and the diameter of the pin was 4 mm. The tool rotation speeds were 750, 825, and 900 rpm, while the tool traverse speeds were 10, 15, and 18 mm/min. FSW was performed with AZ31B placed on the advancing side (AS). The design matrix of the experiment is presented in Table 1. Specimens for optical microscopy were sliced using an electrical discharge machine across the perpendicular cross-section perpendicular to the weld. The joints were prepared and swabbed with different etching solutions (3 g C₆H₃N₃O₇ + 5 ml CH₃COOH + 50 ml C₂H₆O + 10 ml distilled water for the Mg side, and 1.5 ml HCL + 1 ml H.F. + 2.5 ml HNO₃ + 95 ml distilled water for the Al side) until clear and distinct etching was obtained. Ethanol was used to clean the etched samples. The weld's microstructures were examined using an optical and scanning electron microscope (JSM-6460 with Oxford energy dispersive X-ray spectroscopy system). The joint strengths were measured using a universal testing machine (TINIUS OLSEN H25KT) according to the ASTM E8 standard. The specimen dimensions are shown in Fig. 1. Microhardness was measured with a Vickers microhardness tester (Mitutoyo, Model: MVK – H1) under a 200 g load applied for 20 s.

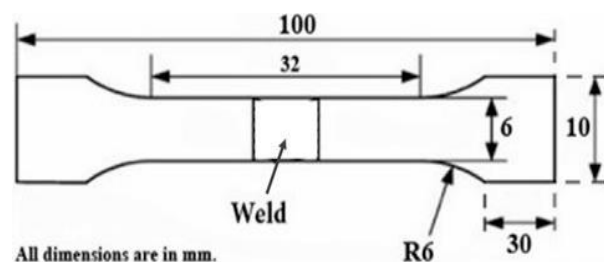


Fig. 1. Dimensions and specifications of tensile specimen

Table 1. Design Matrix and Corresponding Testing Results

SI No	TRS	TTS	SD	Tensile strength (MPa)	Microhardness (HV)
1	750	10	15	103	69
2	900	10	15	126	74
3	750	20	15	130	73
4	900	20	15	121	69
5	750	10	21	114	71
6	900	10	21	135	74
7	750	20	21	97	73
8	900	20	21	121	72
9	750	15	18	146	83
10	900	15	18	167	87
11	825	10	18	148	86
12	825	20	18	139	89
13	825	15	15	170	69
14	825	15	21	171	68
15	825	15	18	182	89
16	825	15	18	180	89
17	825	15	18	177	89
18	825	15	18	178	89
19	825	15	18	179	89
20	825	15	18	180	89

2.1. ANN

This investigation uses Deep Neural Networks (DNN) to model and predict the mechanical properties of Al-Mg dissimilar FSW joints. The primary emphasis is placed on comprehending the influence of diverse hyperparameters, including activation functions, training algorithms, and network structures, to enhance the accuracy of the models. Fig. 2. shows the DNN architecture [28, 29].

The experimental results were normalized for standardization and improved training efficiency. Then the datasets were divided into training (75%), validation (15%), and testing (15%) sets. Bayesian optimization is employed to optimize the parameters of the neural network, including the number and size of hidden layers, the transfer function, and the training function. The hyperparameters taken for Bayesian optimization are defined in Table 2.

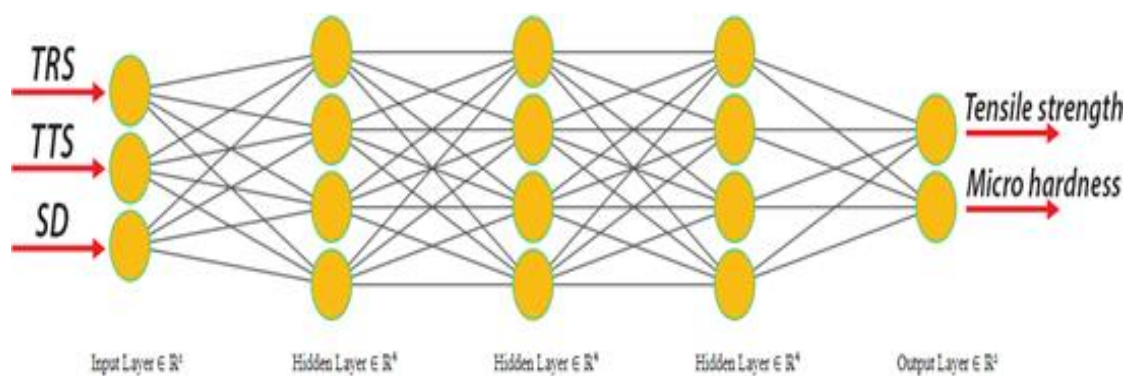


Fig. 2. Deep Neural Network (DNN) Structure and Layer Composition

Table 2. Hyperparameter Configuration for Bayesian Optimization

Hyperparameter	Range
Hidden layers	1-5
Hidden Neurons	5-15
Transfer functions	Tansig, Logsig & Poslin
Training function	Trainlm, Traingdx & Trainsg

The training procedure is directed at minimizing MSE, serving as the specified objective function Fig. 3 delineates the evolution of the Bayesian optimization process with the algorithm striving to diminish MSE. Two distinct trajectories are depicted in the graph. The blue trajectory chronicles the smallest value of the objective function that has been encountered after each function evaluation. Notably, this trajectory descends stepwise with the identification of each new, lower minimum. The green trajectory embodies the algorithm's predictive assessment regarding the potential lowest point (nadir) of the objective function. As the process matures, a convergence is observed between the estimated and actual minimum objectives, underscoring a burgeoning confidence in the optimization's prediction of the minimum's locus.

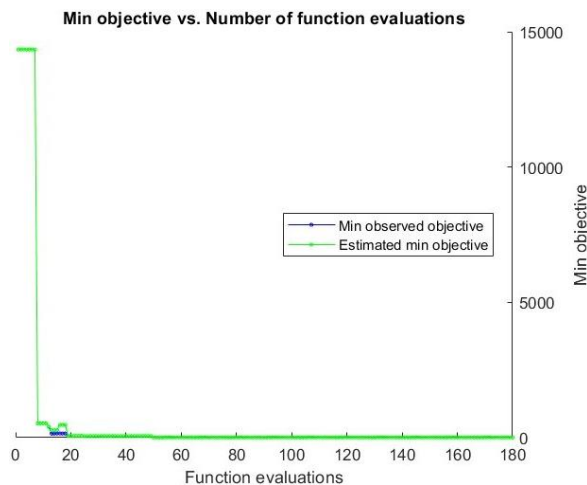


Fig. 3. Evolution of Bayesian Optimization for MSE Reduction

A heatmap of the mean squared error (MSE) for various configurations of a neural network is shown in Fig. 4. The results presented in this heatmap serve as a basis for selecting the best-performing neural network configuration for further testing or deployment. As determined by Bayesian optimization, the best-performing comprises a neural network architecture with four hidden layers, each consisting of 11 nodes. The selected transfer function is 'poslin' (positive linear) for the hidden layers, and the training function is 'trainlm' (Levenberg-Marquardt backpropagation). Optimized hyperparameters resulting from Bayesian optimization are used to build the neural network, and then the neural network is trained. The trained artificial neural

network (ANN) is assessed by measuring its performance using the RMSE and R^2 values. The performance plot is shown in Fig. 5 shows the mean squared error (MSE) on a logarithmic scale for three different datasets training, validation, and test over 22 training epochs. The training data's error (blue line) consistently decreases, showing the network is learning from the training data. The validation data's error (green line) decreases until epoch 16, where it reaches its minimum MSE of 37.0807, suggesting the optimal stopping point to prevent overfitting. The test data's error (red line) shows the network's performance on unseen data, which follows a similar trend to the validation data, providing insight into the model's generalization capability.

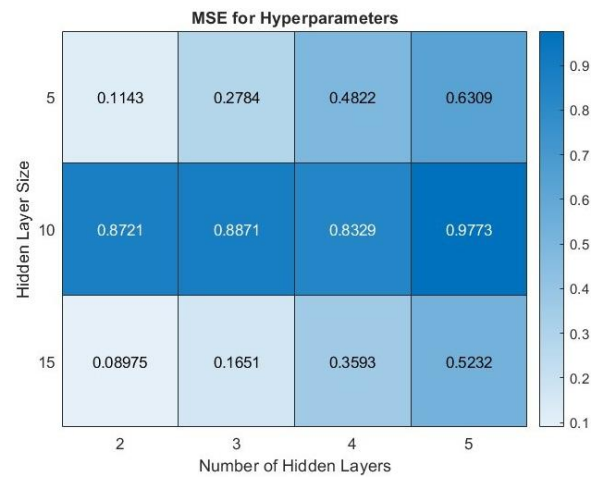


Fig. 4. MSE Heatmap for Hidden Layer Configurations

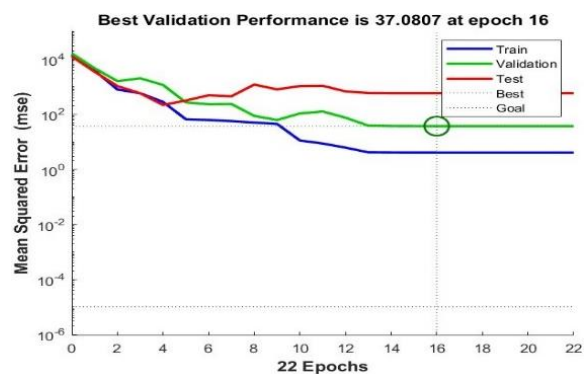


Fig. 5. Performance Evaluation of Trained Deep Neural Network (DNN) using RMSE and R^2 Values

Fig. 5 encapsulates the training phase's dynamics, indicating effective learning while also suggesting the onset of overfitting past the 16th epoch, as seen by the upturn in validation error. This inflection point is critical for model

selection, as it marks the transition from learning to overfitting, emphasizing the importance of early stopping in neural network training. The efficiency of the neural network was assessed using RMSE, R^2 , and the correlation coefficient (R). These metrics are summarized in Table 3.

3. RESULTS AND DISCUSSION

Fig. 6 shows the regression plot of the network performance. The overall R-value, a correlation measure, reached an impressive 0.97203. Moreover, individual values for training (0.998), validation (0.99), and test (0.89) datasets

demonstrate the generalization capability of the model. The comparison of experimental and predicted tensile strengths and hardness is presented in Fig. 7 (a & b). The model predictions closely align with the experimental values, and hypothesis tests indicate that the experimentally determined tensile strength and the model predictions exhibit statistically equivalent means. Specifically, the apex tensile strength, both predicted and experimentally found, stands at 179.26 MPa, corresponding to a TRS of 825 rpm. Conversely, the experimental nadir of tensile strength is noted at 97 MPa, with the model predicting a slightly higher minimum of 103 MPa.

Table 3. Metrics for Assessing Neural Network Efficiency

Performance evaluation Parameter	Value
RMSE	13.2877 & 4.10232
R^2	0.94858
Correlation Coefficient (R)	0.97203

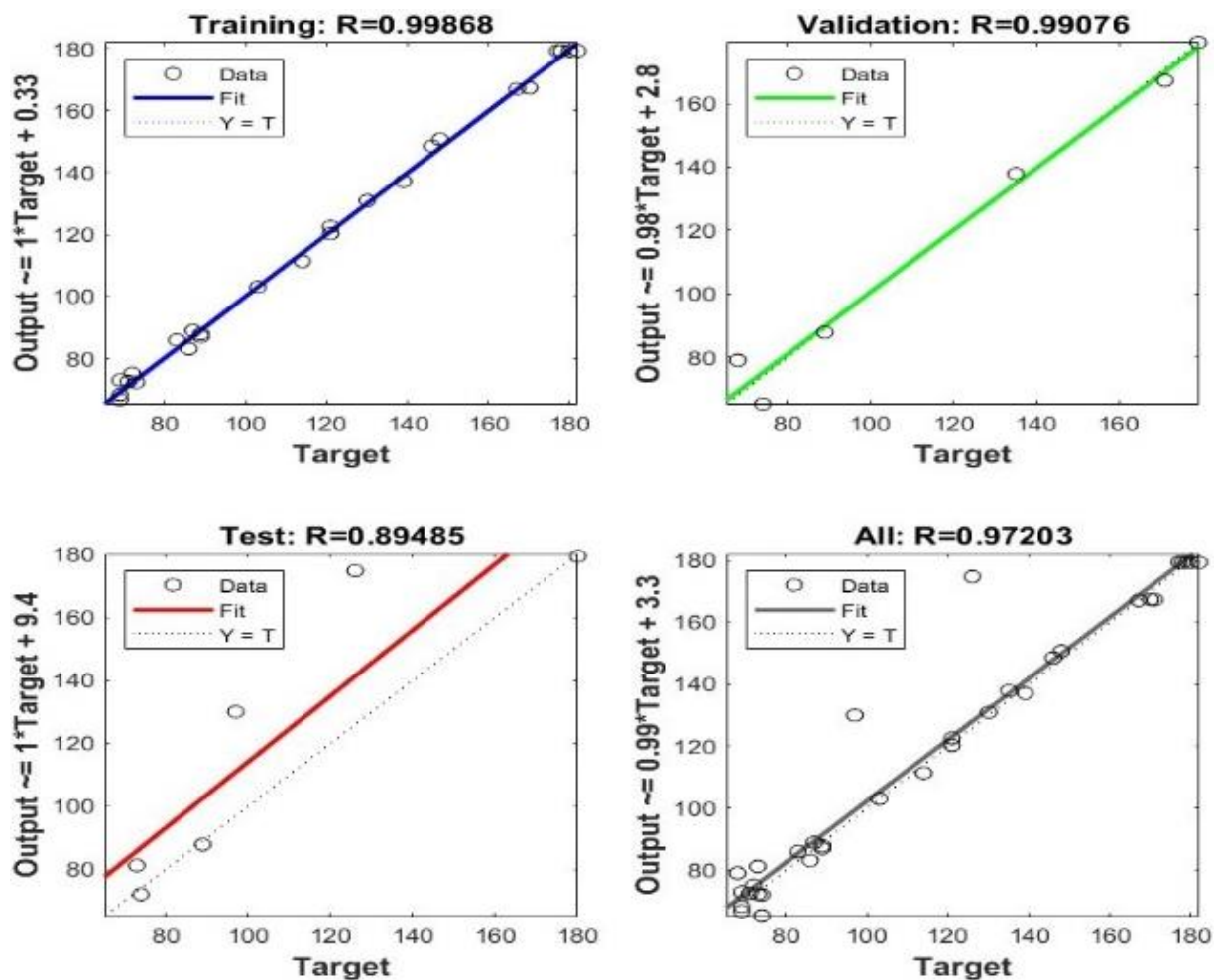


Fig. 6. Comparison of DNN Predicted Outputs with Actual Values across Training, Validation, Testing, and Target Sets

The mean of the experimentally tensile strength, which is 148.2 MPa, is closely mirrored by the model's prediction of 152.01 MPa.

The model predicts a maximum microhardness value of 90 HV, which matches the experimental result achieved for the joint created with a tool rotation speed of 825 rpm. The lowest microhardness value obtained from experiments is 69 HV, while the lowest Microhardness predicted is 68 HV. The mean Microhardness of the joints is found as 79.55 HV, while the predicted average Microhardness is 81.12 HV.

3.1. Effect of Parameters on Tensile Strength and Microhardness

The investigation, illustrated in Figures 8 to 14, provides insights into the intricate relationships between parameters and their effects on the joints' tensile strength (TS) and Microhardness (MH). Fig. 8 shows that an 18 mm shoulder diameter, with a TRS increase from 800 to 900 rpm and lower TTS, optimally achieves a peak tensile strength of 190MPa. However, Fig. 8 reveals that beyond a certain point, TS diminishes due to challenges such as suboptimal material flow and excessive heat.

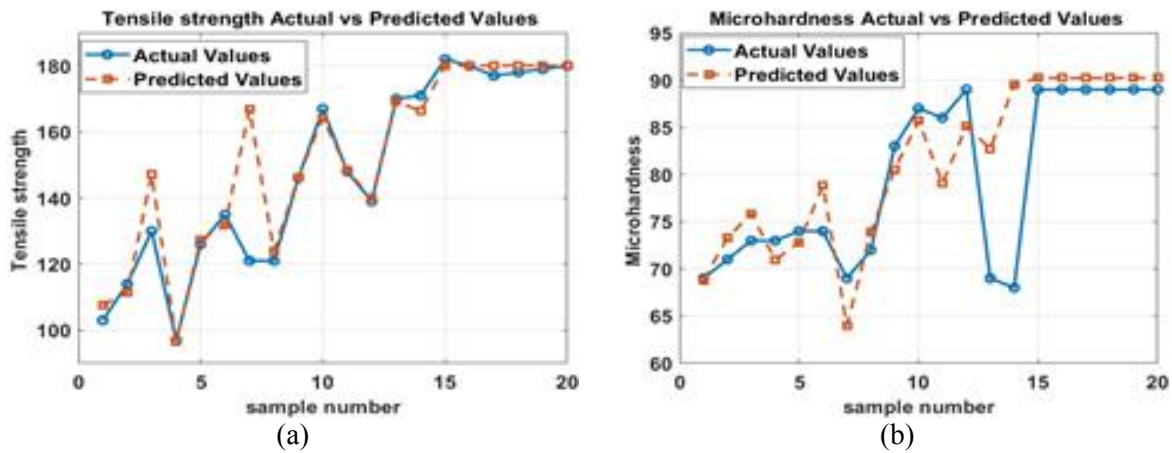


Fig. 7. Comparison of Experimental and Predicted (a) Tensile Strength and (b) Micro Hardness

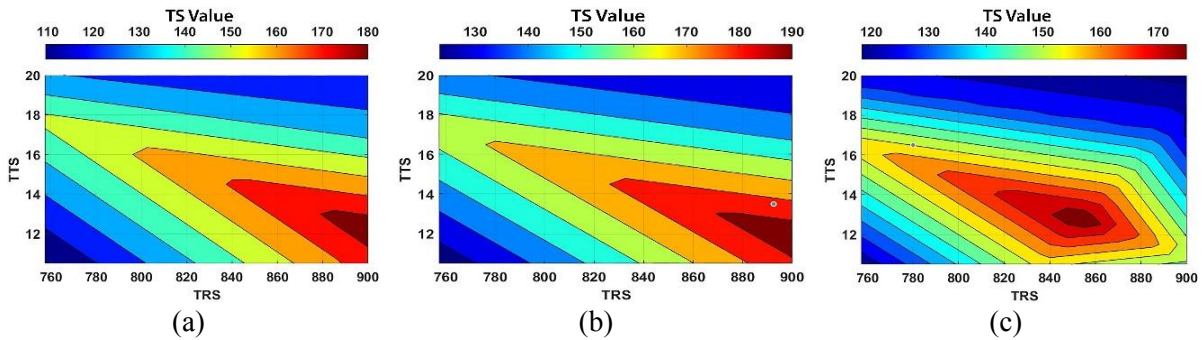


Fig. 8. Influence of TRS and TTS on Tensile Strength Across Various SD (a) 15 mm, (b) 18 mm, and (c) 21 mm

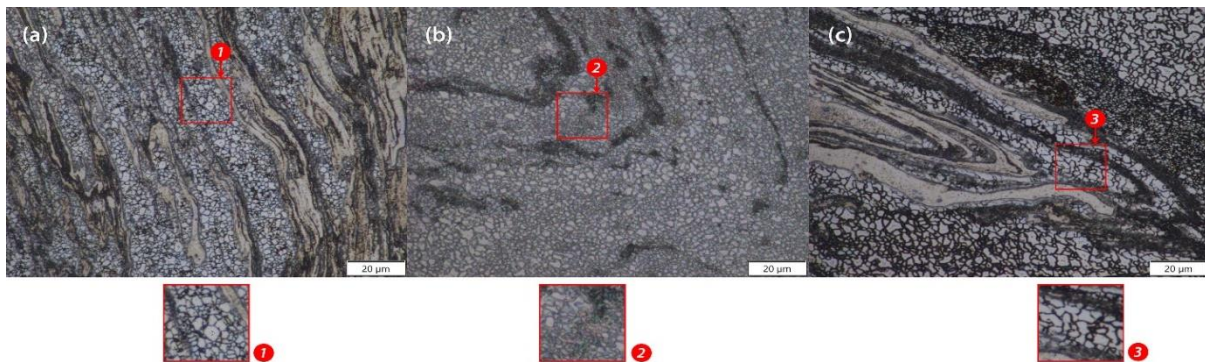


Fig. 9. Microstructures of Stir Zone at TTS of 15 mm/min, SD of 18 mm, and TRS of a) 750 rpm, b) 825 rpm, c) 900 rpm

Examining the impact of TRS on stir zone grain size (Fig. 9), we observe notable grain coarsening within the AZ31B nugget at high rotation speeds, ascribed to the annealing effect caused by heat generated during welding. Considering the microstructures from regions 1, 2, and 3 corresponding to 750 rpm, 825 rpm, and 900 rpm respectively, it is evident that grain coarsening is more pronounced in the microstructure obtained at 900 rpm. The increase in temperature of the nugget, caused by increased frictional heat and plastic deformation during FSW, leads to the expansion of grains as the TRS (tensile residual stress) increases. These findings are in alignment with Firouzdor et al., who reported that joint strength escalates with an increase in traverse speed up to a certain threshold, beyond which a reduction is experienced [13]. This phenomenon's underlying mechanism is grain coarsening and premature aging processes. Microhardness, as depicted in Fig. 10, exhibits a similar trend, increasing with rising TRS and TTS until a threshold, beyond which it declines due to heat input variations affecting the weld's hardness compared to the base material. The highest Microhardness, around 90 HV, is achieved with an 18 mm tool shoulder diameter. Initially, as SD increases from 15 mm to 18 mm, the microhardness increases with increasing TRS and TTS due to enhanced material flow and grain refinement facilitated by higher heat input.

This leads to increased dislocation density and grain boundary strengthening, consequently increasing the microhardness. However, when SD further increases to 21 mm, although the TRS and TTS remain in the range associated with higher hardness, the peak hardness is achieved at relatively lower TRS and TTS values compared to the maximum observed for the 18 mm SD. This phenomenon can be attributed to the

interplay of heat input variations and material flow dynamics. At 21 mm SD, the increased heat input might result in excessive thermal softening, counteracting the beneficial effects of grain refinement, and thereby limiting the hardness improvement. Fig. 9 further emphasizes that samples with reduced tool rotation and traverse speeds display hardness fluctuations due to diverse constituents and the creation of IMCs in the area where stirring occurs. Brittle intermetallic compounds increase hardness, while improper heat input during welding can result in the recrystallization of Al/Mg grains, potentially lowering hardness. Fig. 11 & Fig. 12 explore the combined impact of tool transverse speeds (TTS) and tool shoulder diameters (SD) on tensile strength and Microhardness. Initial increases in TTS and SD improve tensile strength up to a moderate level, but further increments lead to a decline. Microhardness, correlated with welding speed, initially increases but reverses beyond specific TTS and SD thresholds. Fig. 13 & Fig. 14 delve into the intricate influence of tool rotation speeds (TRS), shoulder diameters (SD), and constant tool transverse speeds (TTS) on tensile strength and Microhardness. Moderate values of TRS and SD initially boost tensile strength, but a subsequent decline occurs with further increases. Microhardness reaches its maximum (90 HV) with elevated TRS, moderate SD, and high TTS.

3.2. The Formation of IMCs and its Impact on the Characteristics.

The interface microstructures of the joints produced under parameter combinations categorized as low (TRS= 750 rpm, TTS= 10 mm/min, SD= 15 mm), middle- (TRS= 825 rpm, TTS= 15 mm/min, SD= 18 mm), and high (TRS= 900 rpm, TTS= 20 mm/min, SD= 21 mm) are illustrated in Fig. 15.

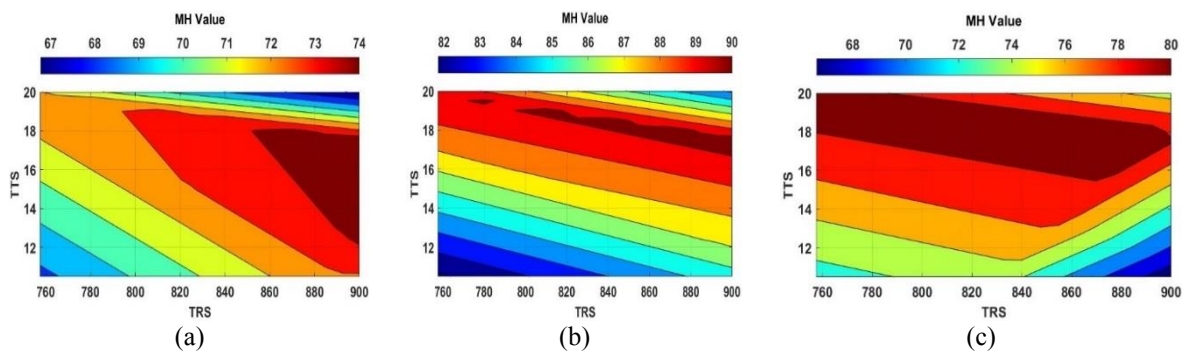


Fig. 10. Influence of TRS and TTS on Microhardness across Various SD (a) 15 mm, (b) 18 mm, and (c) 21 mm

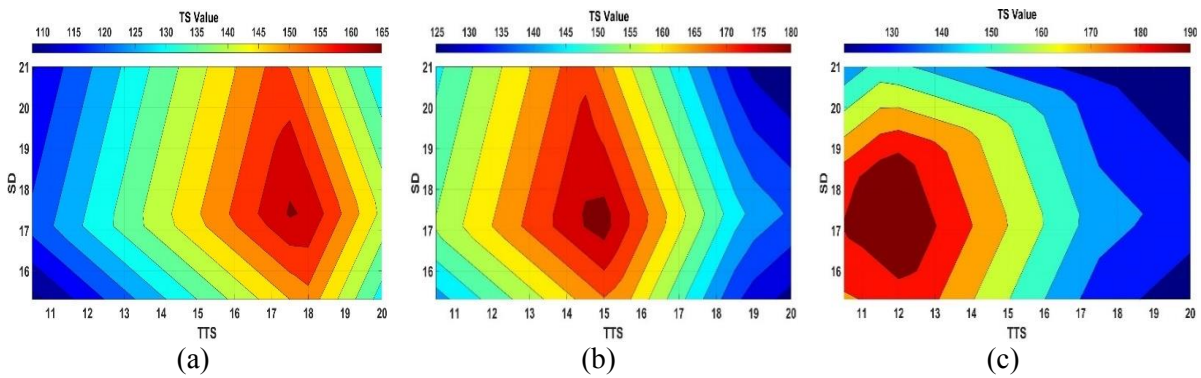


Fig. 11. Influence of TTS and SD on Tensile Strength across Various TRS (a) 750 rpm, (b) 825 rpm, and (c) 900 rpm

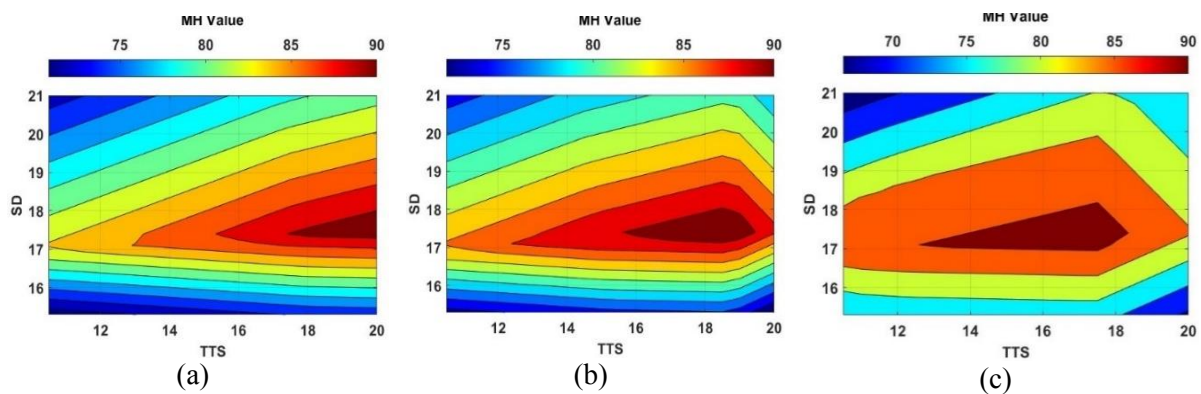


Fig. 12. Influence of TTS and SD on Microhardness for TRS of (a) 750 rpm, (b) 825 rpm, and (c) 900 rpm.

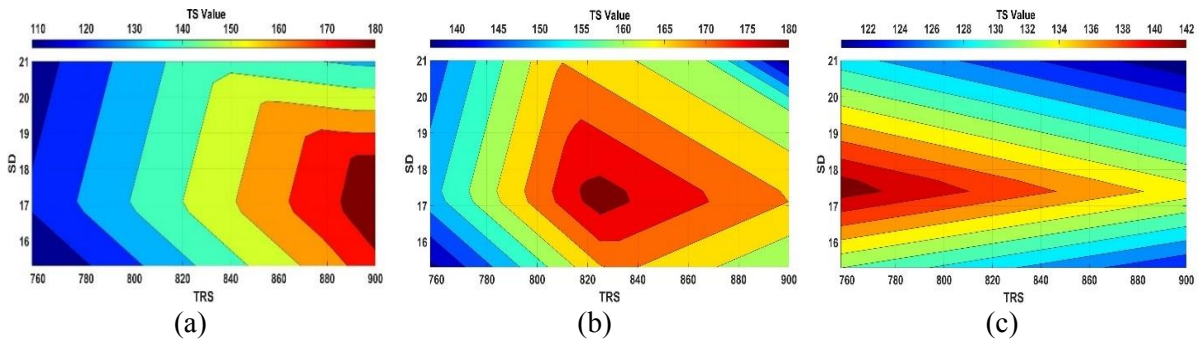


Fig. 13. Influence of SD and TRS on Tensile strength for TTS of (a) 10 mm/min, (b) 15 mm/min, and (c) 20 mm/min

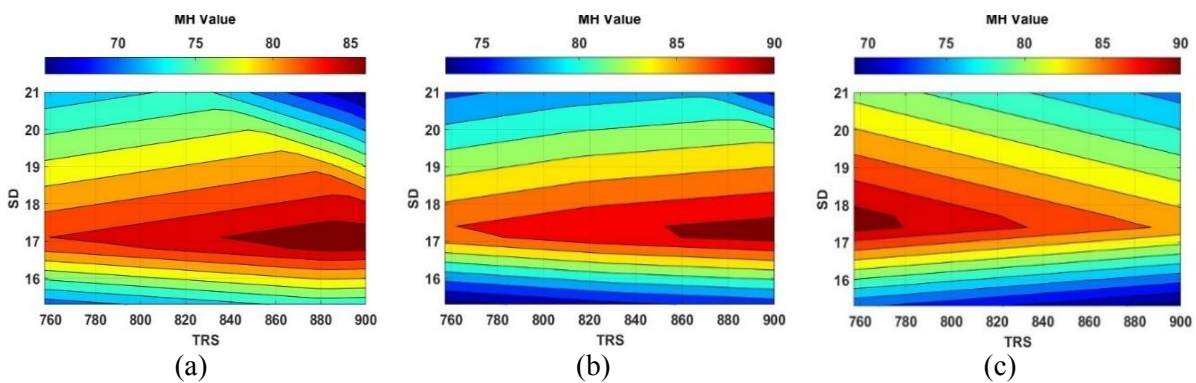


Fig. 14. Influence of SD and TRS on Microhardness for TTS of (a) 10 mm/min, (b) 15 mm/min, and (c) 20 mm/min

The interface microstructure exhibits a banded configuration, characterized by two bands with disparate contrasts. The lamellae consist of distinct phases formed during the turbulent amalgamation of two alloys, resulting in an intercalated structure. Plastic deformation induces the formation of alternating layers of Mg and Al deposits in the weld center. The optimum intercalated structure is achieved with the middle parameter combination, whereas other parameter sets exhibit reduced intercalated and banded structures. Analysis of the micrograph suggests that the heat generated during this specific parameter combination is conducive to the even distribution of intermetallic elements and mutual diffusion of Al and Mg atoms.

The interface microstructure shown in Fig. 16(a) & (b) highlights the existence of different intermetallic phases. EDS line analysis was performed over the interface zone of the joint made with the medium parameter combination to determine the phases generated during FSW. Fig. 17 shows two contrasts for two different bands that form the Microstructure. The EDS conveys that the intermetallic compounds $Al_{12}Mg_{17}$ and Al_3Mg_2 are developed during welding.

3.3. Quantitative Analysis of Microstructure and Influence on Properties

A quantitative study of the microstructures of joints welded with low, middle, and high

parameters was performed to explore the change in grain size. The micrographs ($20 \times 20 \mu\text{m}$) used for the analysis are shown in Fig. 18. The number of grains in the micrograph measured using the line intercept methods is given in Table 4.

The results show that the grain size for middle parameter combinations is $2.23 \mu\text{m}$. The grain sizes for the high and low parameter combinations are $10.5 \mu\text{m}$ and $5.58 \mu\text{m}$, respectively. The intermediate parameter combination significantly reduces the average grain size due to the occurrence of new grains resulting from the heating and plastic deformation of the tool. Azizieh. et al. mention that larger grain size results from the rise in peak temperature, and grain size remains constant above a particular temperature. This is due to the increased liquid content, which decreases frictional heating [19].

As per the Hall-Petch equation, a grain size decrease increases strength and hardness. The reduction in particle size will enhance the hardness of the material. In this scenario, the presence of fine grain in the stir zone leads to a significant increase in Microhardness. The sample of the middle parameter has a grain size of $2.33 \mu\text{m}$, a tensile strength of 180 MPa, and a Microhardness of 88 HV. The grain size for the high parameter combination is $10.5 \mu\text{m}$, resulting in a fall in tensile strength to 120 MPa and a decrease in hardness to 68 HV.



Fig. 15. Stir zone Microstructures for a) low b) middle and c) high parameter combinations

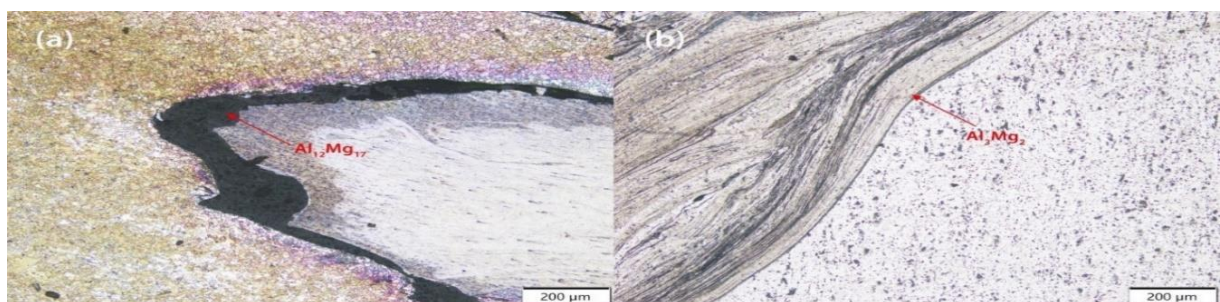


Fig. 16. Interface Microstructures Highlighting Intermetallic Phases on (a) Mg Side and (b) Aluminum Side

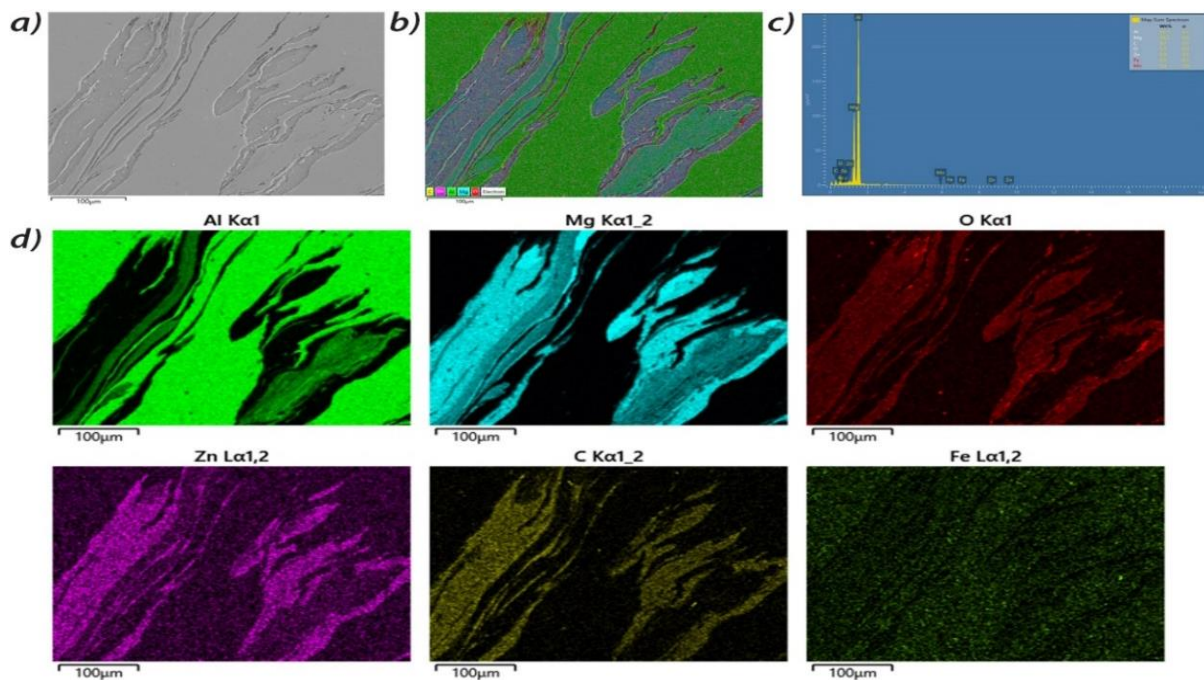


Fig. 17. EDS analysis of sample welded with medium parameters



Fig. 18. Microstructures of Friction Stir Welded Joints: (a) 750 rpm, 10 mm/min, 15 mm, (b) 825 rpm, 15 mm/min, 18 mm, and (c) 900 rpm, 20 mm/min, 20 mm

Table 4. Grain size and count for different parameter combinations

Parameters combination	Number of grains	Grain Size (μm)
Low	153	5.58
Middle	879	2.331
High	43	10.5

4. CONCLUSIONS

Friction stir welding has effectively joined alloys AA5052 to AZ31B using various combinations of tool rotation speeds, tool traverse speeds, and shoulder diameters. The joint qualities were investigated using microstructural characterization, tensile testing, and microhardness studies. A neural network model was developed to forecast the tensile strength and Microhardness in friction stir welding. The observations are summarized below:

- Deep neural network (DNN) was employed to

forecast the tensile strength and microhardness of the joint. Hyperparameter optimization was performed using Bayesian optimization. The overall coefficient of correlation, denoted as R , is 0.97. The outcomes derived from employing Artificial Neural Networks (ANN) are closely aligned with the results gained through experimental testing. The little disparity between the forecasted artificial neural network (ANN) model and empirical data indicates the dependability of this model.

- The Microstructure of the base material and joints were examined. The formation of

lamellae, which is made of distinct phases due to the improper mixing of the alloys, results in the formation of a banded structure. Interface microstructure demonstrates the existence of intermetallic compounds.

- At greater tool rotation speeds, annealing leads to substantial enlargement of the grain size. The AZ31B base material has a grain size of 10 μm. Particles with a diameter of 2.23 μm are produced by using a rotational speed (TRS) of 825 rpm, a traverse speed (TTS) of 15 mm/min, and a sample distance (SD) of 18 mm.
- The tensile test results show that the medium parameter combination results in a joint tensile strength of 180 MPa, while the tensile strength is low for high and low parameter combinations.
- The hardness of the specimen fabricated at the high tool rotational speed is high. Due to excessive liquation and inadequate material flow, no acceptable welds could be produced when TRS was extremely high or extremely low.

TABLE OF ABBREVIATIONS

Abbreviation	Meaning
DNN	Deep Neural Network
ANN	Artificial Neural Network
TRS	Tool Rotation Speed
TTS	Tool Transverse Speed
SD	Shoulder Diameter
TS	Tensile Strength
MH	Microhardness
IMC	Intermetallic Compounds

REFERENCES

[1]. Mendes, N., Neto, P., Loureiro, A., Moreira, A.P., “Machines and control systems for friction stir welding: A review.” *Mater Des.* 2016, 90, 256–265.

[2]. Joost, W.J., “Reducing vehicle weight and improving U.S. energy efficiency using integrated computational materials engineering”. *JOM.* 2012, 64, 1032–1038.

[3]. Joost, W.J., Krajewski, P.E., “Towards magnesium alloys for high-volume automotive applications”. *Scr Mater.* 2017, 128, 107–112.

[4]. Baghdadi, A.H., Mohamad Selamat, N.F., Sajuri, Z., “Effect of tool offsetting on microstructure and mechanical properties dissimilar friction stir welded Mg-Al

alloys”. In: *IOP Conference Series: Materials Science and Engineering.* Institute of Physics Publishing, 2017.

[5]. Raval SK, Judal KB., “Recent advances in dissimilar friction stir welding of aluminum to magnesium alloys”. *Materials Today: Proceedings*, 22, 2020, 2665-75.

[6]. Bisadi, H., Tavakoli, A., Tour Sangsaraki, M., Tour Sangsaraki, K., “The influences of rotational and welding speeds on microstructures and mechanical properties of friction stir welded Al5083 and commercially pure copper sheets lap joints”. *Mater Des.*, 2013, 43, 80–88.

[7]. Zhang, J., Shen, Y., Yao, X., Xu, H., Li, B., “Investigation on dissimilar underwater friction stir lap welding of 6061-T6 aluminum alloy to pure copper”. *Mater Des.*, 2014, 64, 74–80.

[8]. Liu, Z., Ji, S., Meng, X., “Joining of magnesium and aluminum alloys via ultrasonic assisted friction stir welding at low temperature”. *International Journal of Advanced Manufacturing Technology.*, 2018, 97, 4127–4136.

[9]. Kumar Rajak, D., Pagar, D.D., Menezes, P.L., Eyvazian, A., “Friction-based welding processes: friction welding and friction stir welding”, *Journal of Adhesion Science and Technology*, 2020, 34(1), 1-25.

[10]. Fazel-Najafabadi, M., Kashani-Bozorg, S.F., Zarei-Hanzaki, A., “Dissimilar lap joining of 304 stainless steel to CP-Ti employing friction stir welding”. *Mater Des.*, 2011, 32, 1824–1832.

[11]. Heidarzadeh, A., Radi, A., Yapici, G.G., “Formation of nano-sized compounds during friction stir welding of Cu–Zn alloys: effect of tool composition”. *Journal of Materials Research and Technology.*, 2020, 9, 15874–15879.

[12]. Padmanaban, R., Balusamy, V., Vaira Vignesh, R., “Effect of friction stir welding process parameters on the tensile strength of dissimilar aluminum alloy AA2024-T3 and AA7075-T6. *Journal of Engineering Science and Technology*”, *Materwiss. Werksttech*, 2020, 51, 17–27.

[13]. Firouzdor V, Kou S., “Al-to-Mg friction stir welding: effect of material position, travel speed, and rotation speed”.

- Metallurgical and Materials Transactions A., 2010, 41, 2914-35.
- [14]. Malarvizhi, S., Balasubramanian, V., "Influences of tool shoulder diameter to plate thickness ratio (D/T) on stir zone formation and tensile properties of friction stir welded dissimilar joints of AA6061 aluminum–AZ31B magnesium alloys". *Mater Des.*, 2012, 40, 453–460.
- [15]. Fu, B., Qin, G., Li, F., Meng, X., Zhang, J., Wu, C., "Friction stir welding process of dissimilar metals of 6061-T6 aluminum alloy to AZ31B magnesium alloy". *J Mater Process Technol.*, 2015, 218, 38–47.
- [16]. Padmanaban, R., Ratna Kishore, V., Balusamy, V., "Numerical simulation of temperature distribution and material flow during friction stir welding of dissimilar aluminum alloys". In: *Procedia Engineering*, 2014, 854–863.
- [17]. Kishore, V.R., Arun, J., Padmanabhan, R., Balasubramanian, V., "Parametric studies of dissimilar friction stir welding using computational fluid dynamics simulation". *International Journal of Advanced Manufacturing Technology*, 2015, 80, 91–98.
- [18]. Zhao, H., Yu, M., Jiang, Z., Zhou, L., Song, X. "Interfacial microstructure and mechanical properties of Al/Ti dissimilar joints fabricated via friction stir welding". *J Alloys Compd.*, 2019, 789, 139–149.
- [19]. Azizieh, M., Sadeghi Alavijeh, A., Abbasi, M., Balak, Z., Kim, H.S., "Mechanical properties and microstructural evaluation of AA1100 to AZ31 dissimilar friction stir welds". *Mater Chem Phys.*, 2016, 170, 251–260.
- [20]. Song, Q., Wang, H., Ji, S., Ma, Z., Jiang, W., Chen, M., "Improving joint quality of hybrid friction stir welded Al/Mg dissimilar alloys by RBFNN-GWO system". *J Manuf Process.*, 2020, 59, 750–759.
- [21]. Khoshaim, A.B., Elsheikh, A.H., Moustafa, E.B., Basha, M., Mosleh, A.O., "Prediction of residual stresses in turning of pure iron using artificial intelligence-based methods". *Journal of Materials Research and Technology.*, 2021, 11, 2181–2194.
- [22]. Quarto, M., Bocchi, S., Giardini, C., D'urso, G. "An ANN-based approach for the friction stir welding process intrinsic uncertainty". In: *Materials Research Proceedings.*, 2023, 1067–1074.
- [23]. Prudhvi Sai, P., Roshan Balu, T.M.B., Vaira Vignesh, R., Bhaskara Sastry, C.V., Padmanaban, R., "Artificial neural network models for predicting the corrosion behavior of friction stir processed AA5083". In: *Materials Today: Proceedings.*, 2021, 7215–7219.
- [24]. Ai, Y., Shao, X., Jiang, P., Li, P., Liu, Y., Yue, C., "Process modelling and parameter optimization using radial basis function neural network and genetic algorithm for laser welding of dissimilar materials". *Appl Phys A Mater Sci Process.*, 2015, 121, 555–569.
- [25]. Pal, S., Pal, S.K., Samantaray, A.K., "Radial basis function neural network model based prediction of weld plate distortion due to pulsed metal inert gas welding". *Science and Technology of Welding and Joining*, 2007, 12, 725–731.
- [26]. Pramod R, Kumar GV, Gouda PS, Mathew AT., "A study on the Al₂O₃ reinforced Al7075 metal matrix composites wear behavior using artificial neural networks". *Materials Today: Proceedings.* 2018 5, 11376-85.
- [27]. Tyagi, L., Butola, R., Kem, L., Singari, R.M., "Comparative Analysis of Response Surface Methodology and Artificial Neural Network on the Wear Properties of Surface Composite Fabricated by Friction Stir Processing". *J Bio Tribocorros.* 2021, 7.
- [28]. Wu, S., Ren, J., Zhou, X., Cao, G., Liu, Z., Yang, J., "Comparisons of Different Data-Driven Modeling Techniques for Predicting Tensile Strength of X70 Pipeline Steels". *Transactions of the Indian Institute of Metals.*, 2019, 72, 1277–1288.
- [29]. Deng J, Sun J, Peng W, Hu Y, Zhang D., "Application of neural networks for predicting hot-rolled strip crown". *Applied Soft Computing.*, 2019, 78, 119-31.